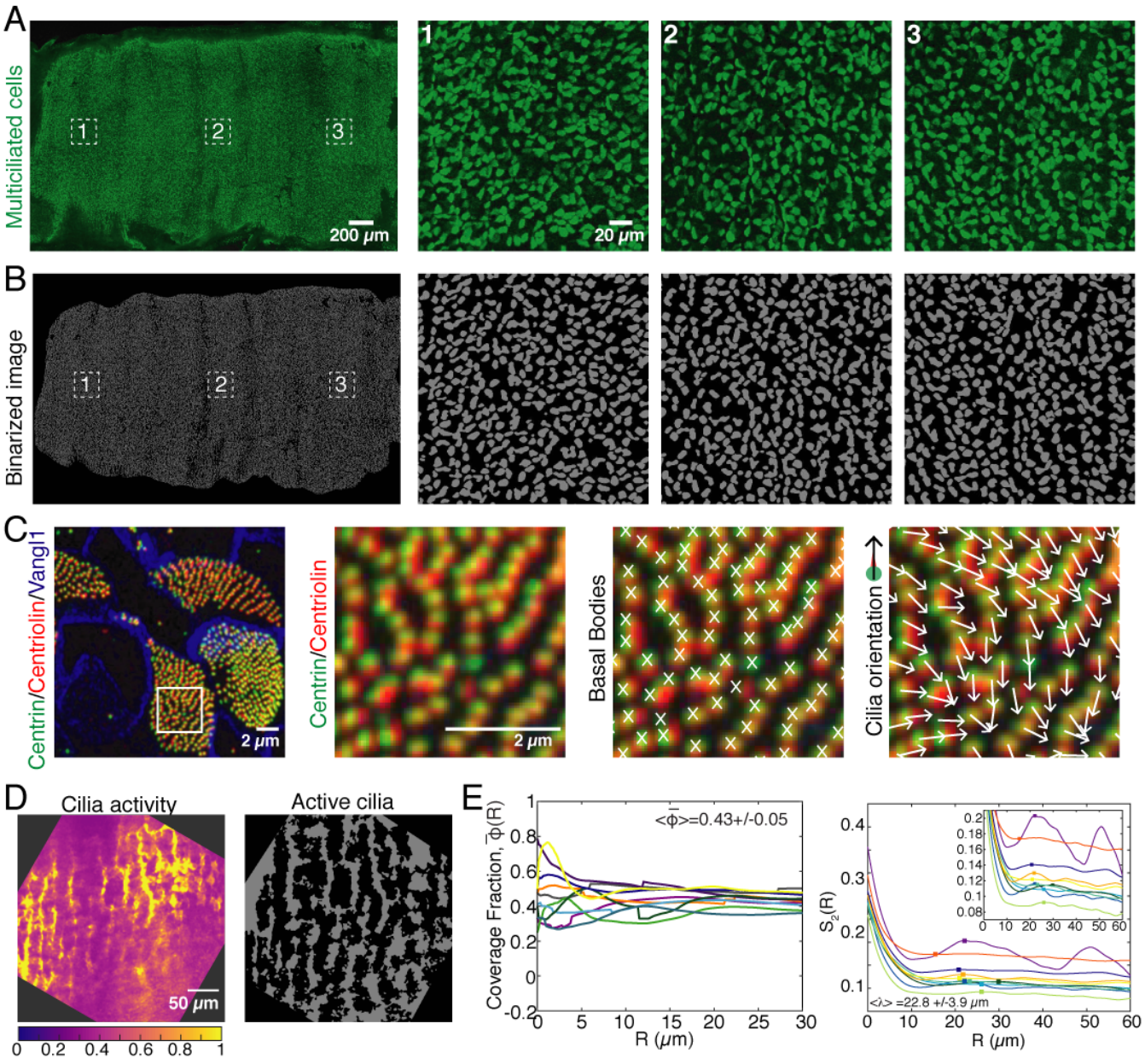

FIG. S1. **A.** Immunofluorescence image of a trachea expressing Centrin-GFP (left). Regions outlined by the squares are magnified to the right, showing that multiciliated cells form a "patchwork" pattern in the distal (1), medial (2) and proximal (3) regions of the trachea. **B.** Binarized images obtained by thresholding images shown in A. **C.** Illustration of cilia orientation analysis. Individual cilia orientation is measured from pairs of Centrin and Centriolin images. First, individual basal bodies (crossed symbols) are identified from Centrin images. Then the cross-correlation function for a pair of Centrin-Centriolin images is calculated in windows of 50 pixels centered around each basal body. The direction of maximum correlation corresponds to the orientation of each cilium (white arrows). **D.** Heat map scaled such the 1 corresponds to the regions of maximum cilia activity in Supp. Video 1. Right: Binary image where white regions show regions where cilia are active in Supp. Video 1 (See Methods § 2 b). **E.** Coverage fraction and wavelength measured by calculating the patial correlation function of binary images where regions with cilia activity were identified (e.g. image shown in D).

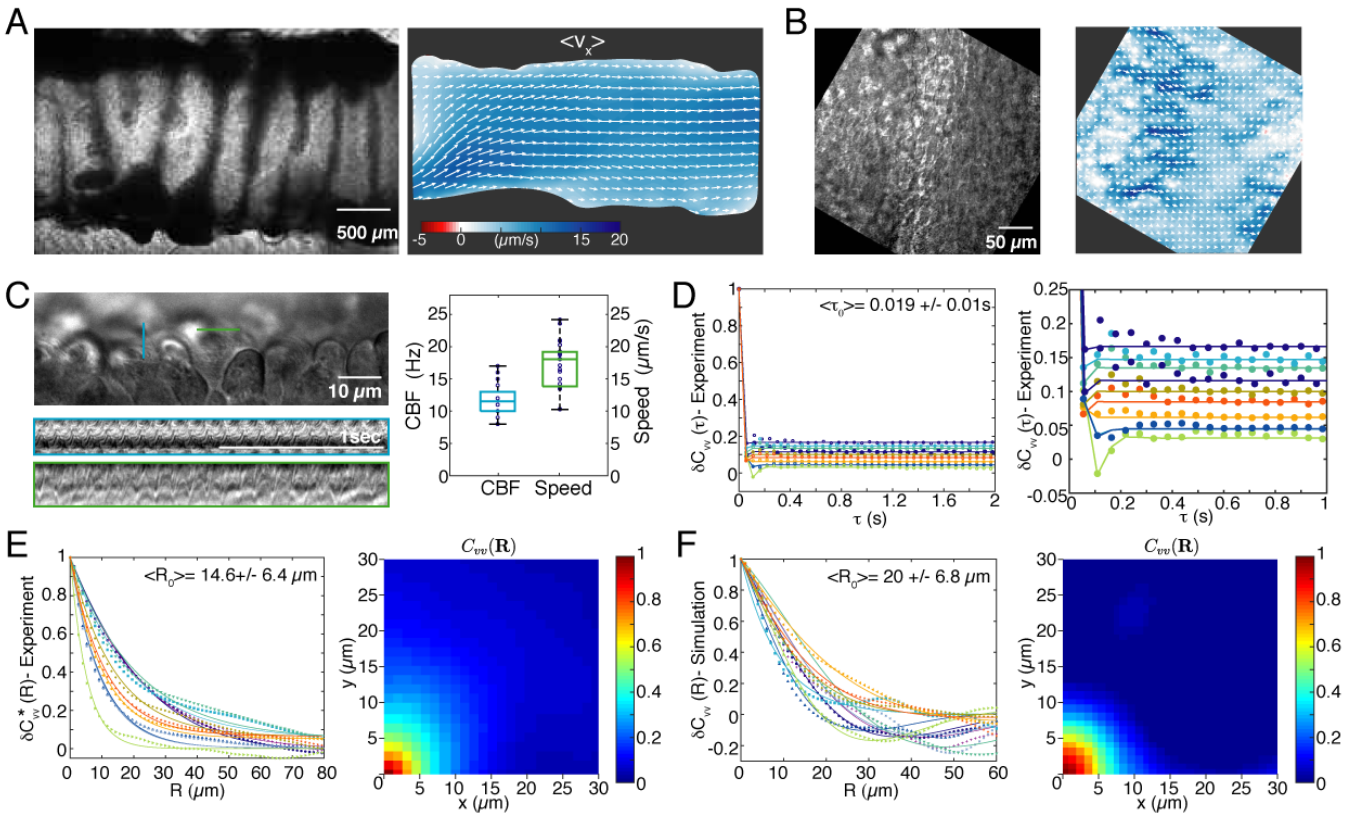

FIG. S2. **A.** Transmitted light image of trachea showing the scale at which flow is measured. Right: Longitudinal flow strength (v_x, red-blue) generated by trachea pictured left. Entire flow strength and streamlines shown in (Fig. 2A,C). **B.** Representative transmitted light image of a typical region of the tissue where flow microstructure is analysed. Right: Longitudinal flow strength (v_x, red-blue) generated by trachea pictured left. Entire flow strength and streamlines shown in (Fig. 2A,C; right). **C.** Quantification of beat frequency and tip velocity of cilia in multiciliated cells. Kymographs drawn from the lines shown in DIC image. Each peak corresponds to one cilia beat cycle (blue), while the slopes of the line indicate the rate at which cilia tips move over time (green). **D.** Plot of temporal correlations of the flow field. Plot on the right shows the region where the $\delta C_{vv}(\tau)$ decays, magnified. Each trace is the correlation function M10 calculated for a field of view of the size shown in B. Points correspond to values measured, solid line shows exponential fits with an oscillatory component (See Methods § 2 d). **E.** Plot of spatial correlations of flow fields measured experimentally. Points correspond to values calculated, solid lines show fits (See Methods 2 d). Right: Heatmap of the two dimensional spatial autocorrelation function $C_{vv}(\boldsymbol{R})$ for the flow field shown in Figure 2C (right panel). **F.** Plot of spatial correlations of simulated flow fields. Measurements of multiciliated cell organisation were used as an input for these simulations (See Methods § 3 e). Right: Heatmap of the two dimensional spatial autocorrelation function $C_{vv}(\boldsymbol{R})$ for the simulated flow field shown in Figure 2D (right panel).

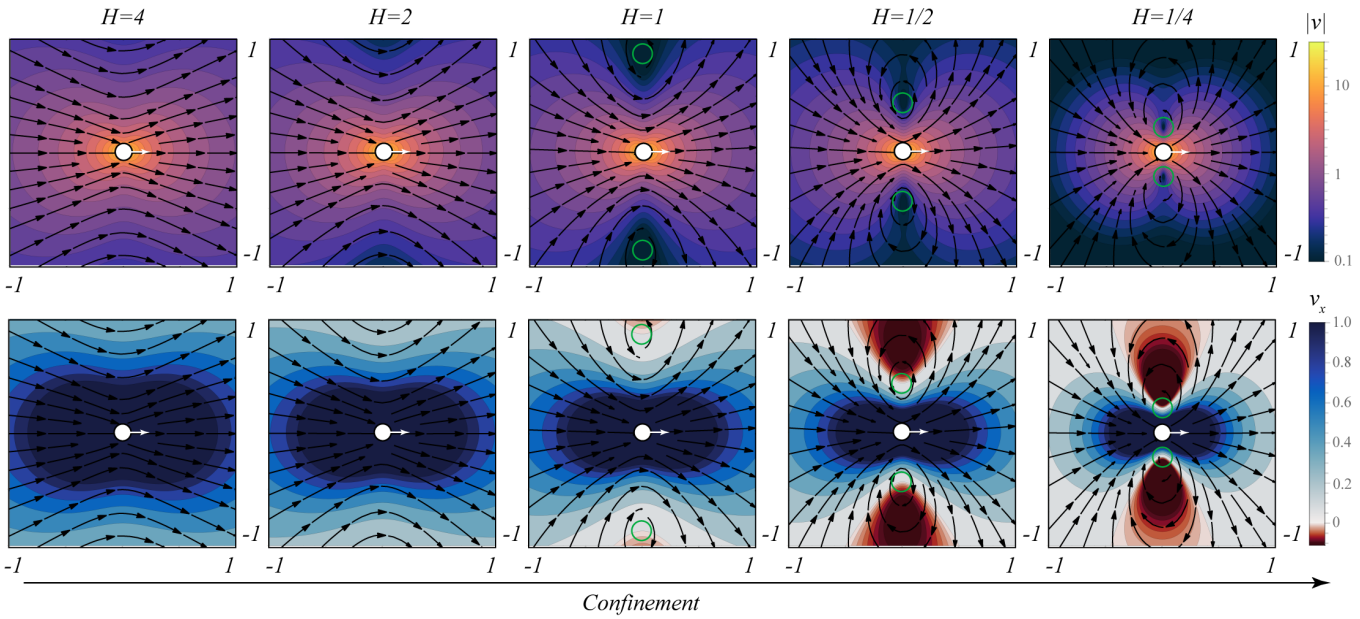

FIG. S3. Effect of confinement on Stokeslet flow in a liquid film. Shown is the analytical solution using 9 image reflections, $(n) = (0) - (9)$ in Table 1 of Mathijssen et al. [49]. The film height in the z direction is H, compared to the horizontal scale $x, y \in [-1, 1]$. The Stokeslets are located in the middle of the film, at $z = H/2$, and oriented in the x direction (white arrows). **Top** panels: Magnitude (thermal) and streamlines (black arrows) of the flow velocity. **Bottom** panels: Same, showing the x component (red-blue) of the flow. For thin films a recirculation emerges, with a vortex centre marked in green.

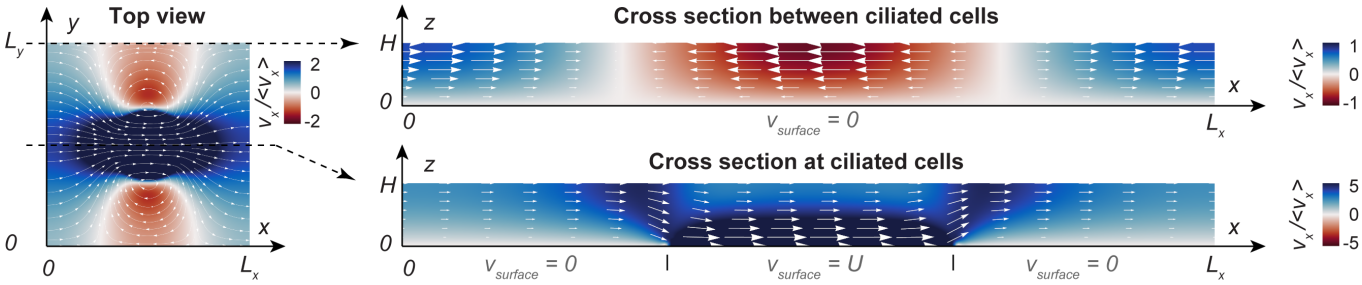

FIG. S4. Three-dimensional structure of the flow generated by a ciliary array, simulated for a square lattice with coverage fraction $\phi = 0.1$, patchiness $\lambda/H = 12.8$, crystallinity $\gamma = 1$ and aligned cilia $\langle p_x \rangle = 1$. The wavelength $\lambda = L = 128\mu$m and the film height $H = 10\mu$m. Shown are streamlines (white) and the longitudinal flow strength (red-blue). **Left.** Top view showing the z-averaged flow velocity, $\bar{\boldsymbol{v}}$, which is the same as Fig. 3D4. **Upper right.** Cross section at $y = 0$ or $y = L$, between the ciliated cells. **Lower right.** Cross section at $y = L/2$, above the ciliated cells.

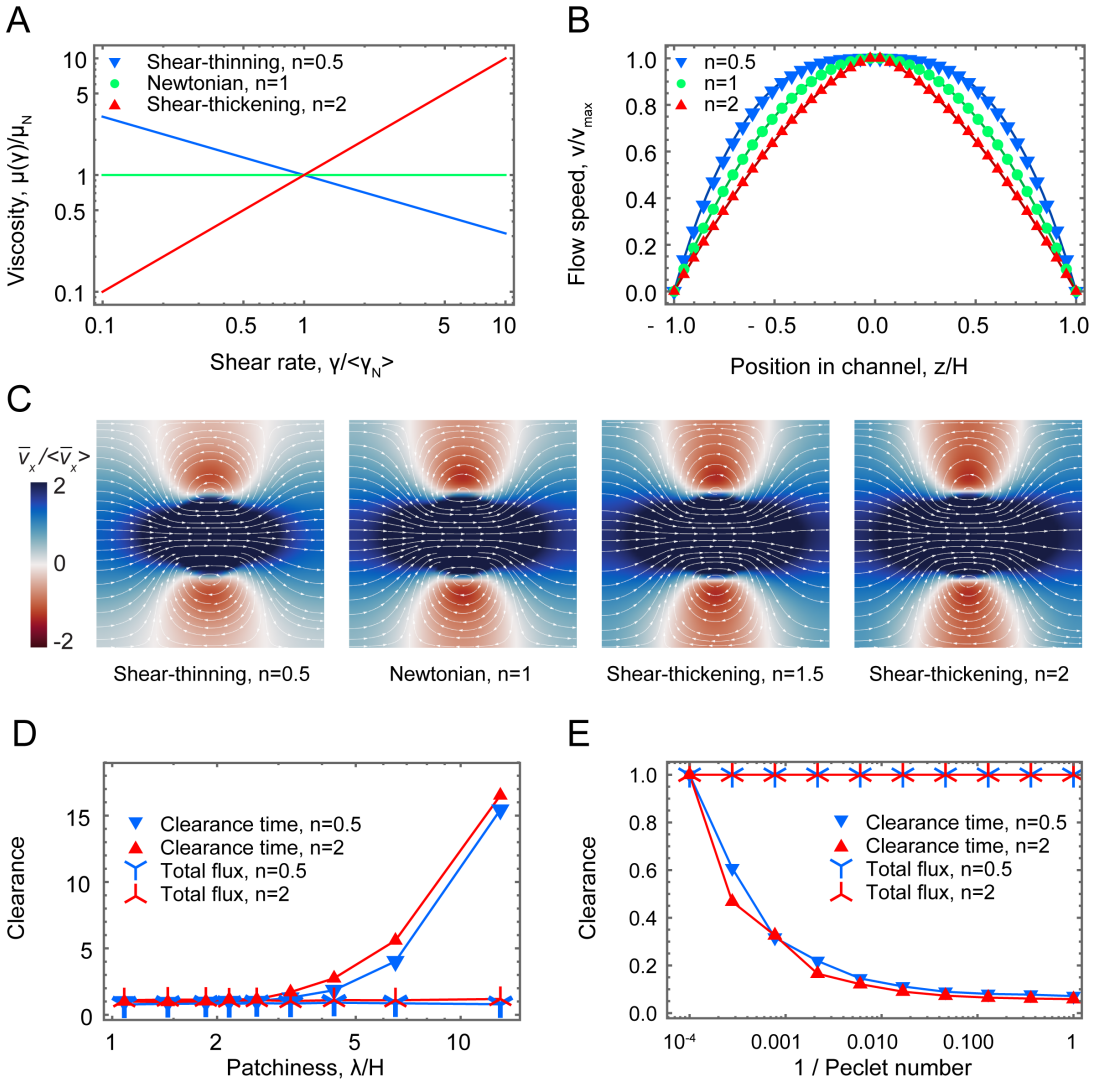

FIG. S5. Effect of shear-dependent viscosity on mucociliary clearance. **A.** Non-Newtonian viscosity μ as a function of shear rate $\dot{\gamma}$ in a power-law fluid (Eq. M26), for a shear-thinning liquid (blue, $n = 0.5$), a Newtonian liquid (green, $n = 1$) and a shear-thickening liquid (red, $n = 2$). **B.** Channel flow velocity profiles for a power-law fluid. Symbols indicate simulated flows with the CFD solver and lines show the theoretical prediction (Eq. M27). For a shear-thinning fluid (blue) the profile is flatter, for a shear-thickening fluid it is sharper (red), and for a Newtonian liquid we recover a parabolic Poiseuille flow. **C.** Flow generated by a ciliary array for different values of the power-law exponent, n, simulated for a square lattice with coverage fraction $\phi = 0.1$, patchiness $\lambda/H = 12.8$, crystallinity $\gamma = 1$ and aligned cilia $\langle p_x \rangle = 1$. Shown are streamlines (white) and the longitudinal flow strength $\bar{v}_x$ normalised with respect to the mean flow $\langle \bar{v}_x \rangle$ of a Newtonian fluid (red-blue), as in Fig. 3D4. **D.** Plot of total flux and clearance time for a shear-thinning (blue) and a shear-thickening fluid (red) as a function of patchiness, normalised with respect to the case of homogeneous coverage ($\lambda = 0$). **E.** Plot of total flux and clearance time for a shear-thinning (blue) and a shear-thickening fluid (red) as a function of Péclet number, normalised with respect to the case of weak noise (Pé $= 10^{-4}$).

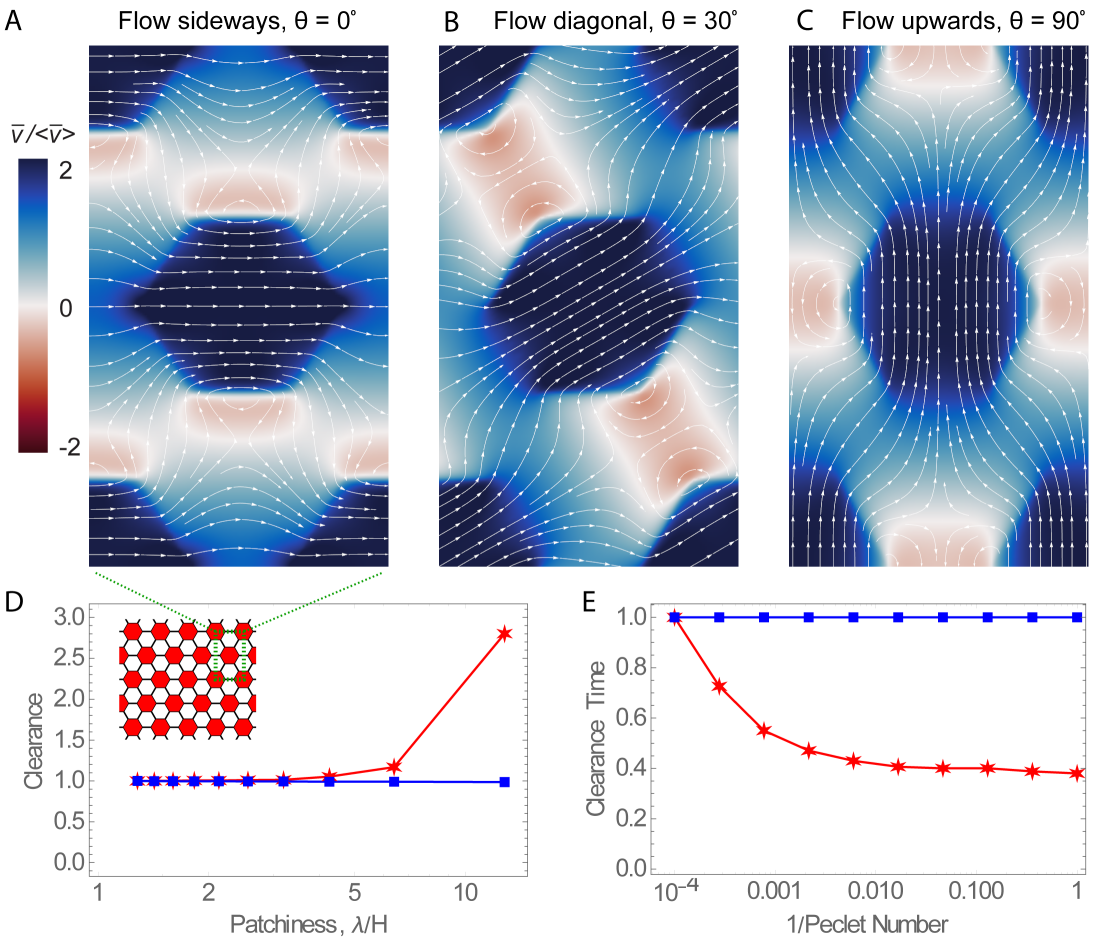

FIG. S6. Total flux and particle clearance for a hexagonal array of ciliary patches. The lattice is shown in the inset of panel D, where red indicates a multiciliated cell. **A.** Simulated flow for cilia oriented in the $\hat{\boldsymbol{x}}$ direction. Shown are streamlines (white) and the longitudinal flow strength (red-blue). The coverage fraction is $\phi = 0.33$, the patchiness is $\lambda/H = 12.8$, the crystallinity $\gamma = 1$ and the cilia are all aligned $\langle p_x \rangle = 1$. **B.** Same, for cilia oriented in the $\theta = \pi/6$ direction. **C.** Same, for cilia oriented in the $\hat{\boldsymbol{y}}$ direction. **D.** Plot of total flux (blue) and clearance time (red) as a function of patchiness, for cilia oriented in the $\hat{\boldsymbol{y}}$ direction, similar to Fig. 3D. **E.** Plot of total flux (blue) and clearance time (red) as a function of Péclet number, for cilia oriented in the $\hat{\boldsymbol{y}}$ direction, similar to Fig. 4C.

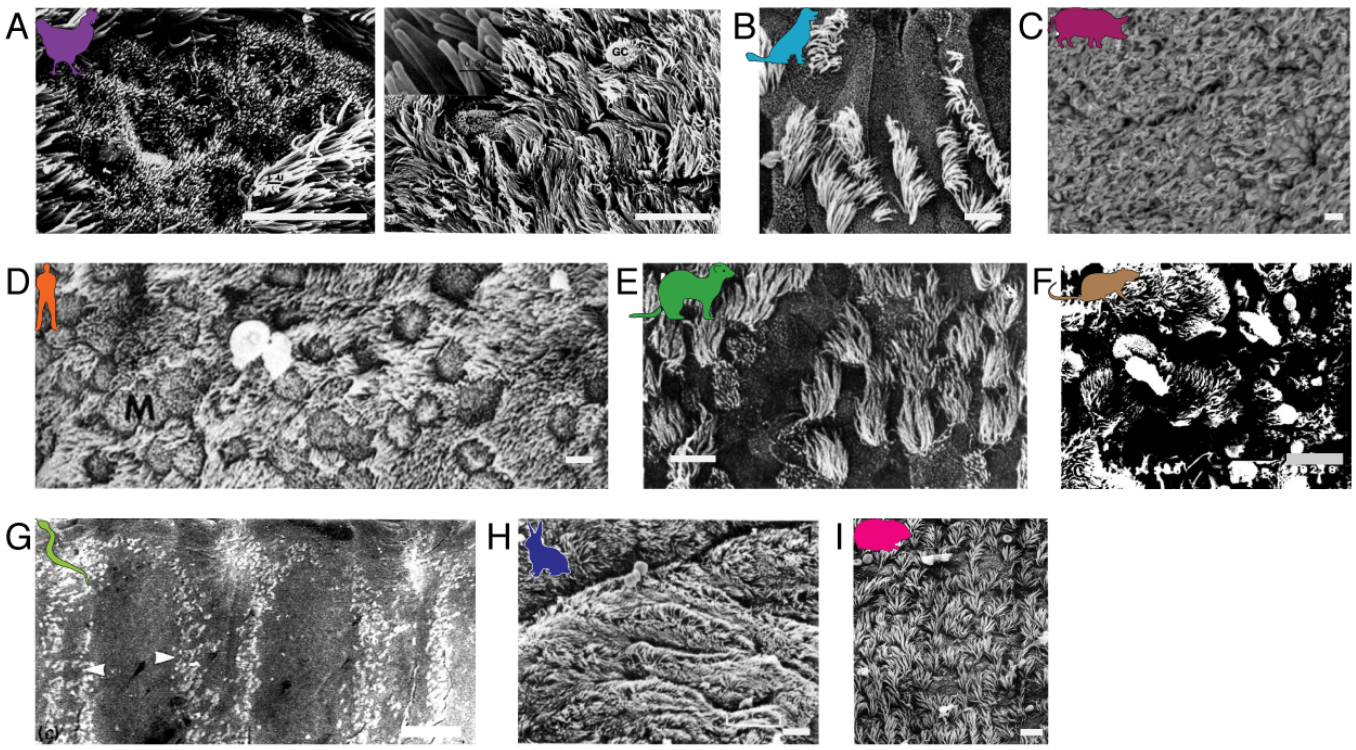

FIG. S7. From the literature: SEM images of airway multiciliated tissue. **A.** Chicken; Image adapted from [39]. **B.** Dog; Image adapted from [40]. **C.** Pig; Image adapted from [45]. **D.** Human; Image adapted from [43]. **E.** Ferret; Image adapted from [41]. **F.** Rat; Image adapted from [47]. **G.** Snake; Scale bar=100μm. Image adapted from [48]. **H.** Rabbit; Image adapted from [46]. **I.** Hamster; Image adapted from [42]. Scale bar=10μm for all panels except G.